Multimedia Tools and Applications
https://doi.org/10.1007/s11042-024-19282-w

New algorithm using an adaptive level set model applied to hippocampus segmentation and volume calculation in MRI images

Boualem Mansouri[1] · Mohammed Chetioui[1] · Catherine Choquet[2] · Lakhdar Boumia[3] · Chama Zouaoui[4]

Received: 8 September 2023 / Revised: 18 March 2024 / Accepted: 22 April 2024

Abstract
The hippocampus is known as one of the most important brain structures since the change in its volume is an early symptom of many diseases such as Alzheimer's disease. Accurate measurement of the hippocampus is very helpful in identifying lesions. Hippocampus segmentation in MRI images is of vital importance for the in-depth study of many brain diseases. However, hippocampus segmentation remains a difficult task due to its small size, complex shape, as well as its imaging characteristics with low contrast and weak and blurred boundaries. To overcome these problems, in this paper, an efficient process is suggested by modeling and solving a system of two-dimensional partial differential equations (PDEs). The first equation allows for restoration using Euler's equation, similar to anisotropic smoothing based on a regularized Perona and Malik filter that removes noise while preserving edge information. The second equation uses the adaptive level set method to segment the image based on the solution of the first equation. This process takes place alternately between these two equations until convergence. This approach allows developing a new algorithm that overcomes the studied model drawbacks. Results of the proposed method give clear segments that can be applied to any application. The proposed method is applied for the hippocampus volume calculation associated with the Scheltens scale. Performance evaluations compared automatic segmentations with manual segmentations performed by expert radiologists. The results revealed a Dice similarity rate average 91.8% and with a volume value varies between 3.19 cm3 and 1.3 cm3 for the right hippocampus in the Scheltens scale, which represents a very significant value compared with other work in the field. Therefore, the method proves clinically useful and effectively segments the hippocampus and gives credibility to the volume calculation, which shows that the developed approach produces superior results in terms of quantity and quality compared to other models already presented in previous works.

Keywords Hippocampus · Image segmentation · Adaptive level set model · Anisotropic smoothing

Extended author information available on the last page of the article

Published online: 03 May 2024

1 Introduction

The hippocampus is a small subcortical cerebral structure, it is an important element of the limbic system of the brain [1], it is located in the medial temporal lobe and plays an important role in human cognition, learning, short-term and long-term memory, and emotional behavior [2–4]. Moreover, it is one of the few regions of the brain in which neurogenesis occurs [5]. Several papers have provided more detailed information showing that the hippocampus is closely linked to human health and disease. Abnormality of this structure is associated with neurodegenerative diseases and brain disorders including Alzheimer's disease [6, 7], epilepsy [8, 9], schizophrenia [10, 11], mild cognitive impairment [12] and major depression [13]. Hippocampal atrophy has been shown to be one of the first observable features for the detection of Alzheimer's disease even at an early stage [14] and [15]. In schizophrenia, symmetry between the left and right hippocampus is used as one of the indicators [16]. The study of hippocampal volume can provide useful results since the volume change is a symptom of many brain diseases. The precise delineation of this structure boundaries makes it possible to obtain a measurement of the volume and to estimate its shape, which can be used to diagnose certain diseases, such as Alzheimer's disease.

Segmentation of the hippocampus in MRI images is of vital importance to aid in the diagnosis. Many clinical applications depend on the results of segmentation of MRI brain structures that allow us to know the changes in brain anatomy during the development of the disease.

The segmentation of the hippocampus in MRI images is one of the major challenges due to its imaging characteristics, with an intensity very close to other adjacent structures, such as the amygdala. The similarity in intensity caused the hippocampus to have faint and fuzzy boundaries. With this challenge a segmentation method that relies solely on image information may not produce accurate segmentation results.

In this paper, our objective is to enhance the precision and quality of hippocampal segmentation by addressing the limitations associated with techniques relying on deformable contours, particularly those utilizing level set methods. We succinctly outline our contributions as follows:

1. Making a compromise between image restoration, edge conservation and correct segmentation by modeling and solving two partial differential equations simultaneously. The first equation allows for restoration that removes noise while preserving edge information. The second equation use adaptive level set method to segments the image based on the solution of the first equation. This process takes place alternately between these two equations until convergence. ensuring a balanced and effective solution.
2. The second novelty in our proposed method involves integrating it with the Scheltens scale for the calculation of hippocampal volume. this association between segmentation and Scheltens scale offer a unique perspective that has not been explored in prior research.

This article is organized as follows: after presenting this introduction, the next section is devoted to related work; the proposed method is presented in Section 3. Section 4 deals with the simulation experiments that justify the contribution of the article to the field applied. Section 5 provides a conclusion on the results obtained.

2 Related Work

We begin this section with a demonstration of automatic segmentation methods for medical images. Since our work focuses on hippocampal segmentation in MRI images using level set methods, we will provide more details on these studies. We will present the drawbacks associated with these methods and discuss previous efforts to mitigate them. Finally, we will introduce our proposed method designed to address these limitations.

2.1 Automatic medical image segmentation methods

In the traditional way, Clustering approaches, such fuzzy mean, are used to achieve image segmentation [17] and Many manually created low-level features, like pixel value distribution and gradient histogram, can be clustered using a genetic algorithm [18]. In image segmentation, probabilistic techniques are also frequently employed.[19–21]. Yingqian Liu and Zhuangzhi Yan in [22] propose a semi-automatic model that combines a deep Learning network and the lattice Boltzmann method for the segmentation of hippocampus. Ferhat Bozkurt et al. in [23] propose A texture-based 3D region growing approach for segmentation in witch they optimizes segmentation parameters through dynamic adjustments informed by texture knowledge. Liu, M et al. propose a multi-model deep learning framework based on convolutional neural network (CNN) for joint automatic hippocampal segmentation and AD classification using structural MRI data [24]. Tao, C. et al. conclude in their paper [25] that the joint training strategy ensures simultaneous optimization of the image synthesis network and the segmentation task, resulting in a more accurate and effective segmentation of the hippocampus in the context of brain tumor radiotherapy planning. A, FP and Liu, Je in [26] proposes a multi-level boundary-aware RUNet segmentation model in order to solve the problem of poor adaptability of deep learning network structures to medical images. Jia-Ni Li et al. in paper [27] proposed a novel cross-layer dual Encoding-Shared Decoding network framework with Spatial self-Attention mechanism (called ESDSA) for hippocampus segmentation in human brains. Considering that the hippocampus is a relatively small part in MRI, thy introduced the spatial self-attention mechanism in ESDSA to capture the spatial information of hippocampus for improving the segmentation accuracy.

A novel method for the automated segmentation of the hippocampus from structural magnetic resonance images (MRI), based on a combination of multiple classifiers is presented by P. Inglese et al. in [28]. Chunming He et al. have introduced innovative methods to improve camouflaged object detection and segmentation. Their FEDER model, detailed in [29], combines traditional detection with an auxiliary edge reconstruction task, resulting in highly accurate object boundaries. In [30], they present the WSCOS method, which addresses intrinsic similarity challenges using a multi-scale feature grouping module to achieve complete segmentation for single and multiple objects. Lastly, their ICEG method, described in [31], enhances detection by extracting internal coherence and employing edge guidance, ensuring more comprehensive segmentation results while eliminating false predictions.

Among the primary difficulties in using automatic medical image segmentation for MRI and CT scans is the defect with imaging process that frequently lead to inconsistencies brightness and contrast levels as well as low sharpness of image of borders.

2.2 Level set models in medical image segmentation methods

On the flip side, deformable active contours serve as an efficient tool for image segmentation and pattern recognition [32–35]. They explicitly represent the object's shape and boundary, combining numerous desirable characteristics. Chen, H et al. in [36] introduces an accurate and robust active contour model to tackle the challenges of intensity inhomogeneity and noise frequently encountered in real medical images.

Level set models, also recognized as geometric deformable models, offer superior solutions to overcome the primary drawbacks of parametric deformable models. The level set method involves initializing a two-dimensional (2D) closed curve or a three-dimensional surface with a potential that permits it to shift at a given speed perpendicular to itself [37]. This approach is employed in image processing as a segmentation tool by evolving a contour based on image properties. In this context, we define an interface C as a level set function of higher dimension. The level set is represented over the rest of the image as the signed distance function from the zero level set, conventionally taking positive values for pixels inside C and negative values for pixels outside C.

However, the level set function often develops irregularities during evolution, causing numerical errors that impact the stability of the level set evolution. To address this, a numerical solution known as re-initialization [38, 39] is introduced, but the challenge arises in determining when and how it should be carried out, affecting numerical precision. Chunming Li et al. proposed Distance Regularized Level Set Evolution (DRSLE) in their paper [40], where the distance regularization effect eliminates the need for reinitialization. Unfortunately, application on real medical images revealed drawbacks in the DRSLE model.

2.3 Disadvantages of the level set in drsle model

The level set model introduced in paper [40], which denotes a regularized form of the model level set, faced the following drawbacks:

1. Li's method is highly sensitive to strong noise and cannot extract edge without gradient or cognitive edges
2. it lacks in one feature that it uses only the edge information from the input image. This leads to incorrect segmentation
3. This model cannot segment in a correct way because it must artificially determine the model's constant evolution speed's symbol based on the location of the initial curve.
4. The edge indicator function g fails to distinguish between the background boundaries and target boundaries. Nonetheless, it is important to note that within a single image, the target boundaries and background boundaries usually exhibit distinct gradient directions.

In their work cited as [41], Y. Wu and C. He introduced a variational level set model featuring an indirect regularization term for image segmentation. They proposed a novel approach to image segmentation by incorporating an indirect regularization term, departing from the conventional practice of directly regularizing the level set function. The authors introduced an auxiliary function to regulate the level set function indirectly. The energy functional in their model consists of a data term, a linking term connecting the level set function and the auxiliary function, and a regularization term for the auxiliary function. Both theoretical and experimental evaluations conducted by authors highlight the advantages of indirect regularization compared to the conventional direct regularization approach.

C. Yu [42] has suggested a novel active contour model (R-DRLSE model) for image segmentation, The R-DRLSE model employs a variational level set strategy, leveraging region information to identify image contours by minimizing the associated energy functional. To streamline the process and eliminate the need for time-consuming re-initialization, a distance regularization term is incorporated to penalize deviations of the level set function from a signed distance function while J. C. Young et al. [43] have introduced a new approach to contour evolution. The study evaluates the use of active contour models, specifically morphological Chan-Vese and morphological Geodesic Active Contour, for segmenting medical images. Results indicate that the morphological Geodesic Active Contour model performs better than Chan-Vese, but both models still fall short of producing segmentation results suitable.

In their work [44], P. Liu and X. Xu improved the conventional distance regularized level set evolution method, introduced new edge indicator functions and presented the Oriented Distance Regularized Level Evolution. This method leverages the directional correlation between the gradient vectors of the level set function and those of the original image to reconstruct the edge map of the original image. Consequently, the impact of undesired strong background boundaries is significantly mitigated and X. Cai [45] has proposed a coupled model for image segmentation and restoration. This study introduces a novel multiphase segmentation model that combines image restoration and segmentation techniques. Leveraging image restoration aspects, the model effectively addresses images with high noise, blurriness, or missing data.

Furthermore, M. Larbi et al. have introduced a novel Level Set Method driven by a New Signed Pressure Force function (SPF) for image segmentation [46]. this paper introduces a novel Level Set Method using a Signed Pressure Force (SPF) function for image segmentation. The method efficiently stops contours at weak or blurred edges and detects exterior and interior boundaries regardless of the initial contour's placement. A comparison with Chan Vese (C-V) model and Geodesic Active Contours (GAC) is conducted, evaluating performance visually and through similarity measurements with reference images..

Despite the advancements in image segmentation using level set functions, a notable challenge persists. The issue of unwanted strong background boundaries. While level set methods have contributed to simplifying and enhancing the accuracy of image segmentation, they have not fully addressed the problem of undesirable strong background boundaries. These persistent artifacts can undermine the precision and reliability of segmentation results, particularly when dealing with complex or intricate images.

In our paper, we propose a novel method that simultaneously addresses a two-dimensional PDE system, striking a balance between image restoration, edge preservation, and accurate segmentation. The first PDE facilitates image restoration by employing a regularized Perona and Malik equation filter, effectively removing noise and preserving edge information in alignment with the detected contours. The second PDE is based on a level set model, utilizing the evolution of a curve propagating in a plane of its normal with a given speed. This evolution is guided by a function that halts the curve at the edges of objects to be detected in the image restored by the first PDE [47].

3 Method

3.1 Formulation and Regularization of the Level Set Model

Equation 1 presents the standard form of the level set equation, where F denotes a directional force acting upon the implicit surface ∅.

$$\frac{\partial \varnothing}{\partial t} = |F \nabla \varnothing| \tag{1}$$

This equation does not have an intrinsic means to maintain regularity, which makes evolution unstable. To remedy this problem, it is necessary to reinitialize periodically on a regular surface. When the implied surface begins to become unstable, the function is reinitialize by solving:

$$\frac{\partial \varnothing}{\partial t} = sign\left(\varnothing_0\right)(1 - |\nabla \varnothing|) \tag{2}$$

The accuracy of this method can be compromised, particularly when dealing with non-smooth implicit surfaces or significant deviations between the signed distance function and the actual surface being reinitialized. Due to these challenges, leveraging a variational approach to derive the evolution equation offers an appealing solution, prized for its simplicity and robustness.

In their paper [40], Chunming Li et al. introduced a novel approach to level set evolution, termed Distance Regularized Level Set Evolution (DRSLE). This technique is formulated through the principles of variational calculus.

A common method for minimizing an energy functional involves finding the steady-state solution to the gradient flow equation.

$$\frac{\partial \varnothing}{\partial t} = -\frac{\partial \varepsilon}{\partial \varnothing} \tag{3}$$

In this case, we substitute the variable ε with an energy functional, which we aim to minimize, this is an energy functional derived using calculus of variation, the partial derivative shown in Eq. 3 becomes a Gâteaux derivative.

The formulation of energy functional is presented as follows:

$$\varepsilon(\varnothing) = \mu R_p(\varnothing) + \varepsilon_{ext}(\varnothing) \tag{4}$$

3.2 External energy

In Eq. 4 ε_{ext} represent the external energy term that derives from an active contour model, leveraging edge-based data. It comprises two intertwined components, operating collaboratively to guide the contour's evolution:

$$\varepsilon_{ext}(\varnothing) = \lambda \mathcal{L}_g(\varnothing) + \alpha \mathcal{A}_g(\varnothing) \tag{5}$$

where $\lambda > 0$, $\alpha \epsilon \mathcal{R}$ constants, the terms $\mathcal{L}_g(\varnothing)$ and $\mathcal{A}_g(\varnothing)$ are defined by: $\mathcal{L}_g(\varnothing) \triangleq \int_\Omega g\delta(\varnothing)|\nabla \varnothing| dx$ and $\mathcal{A}_g \triangleq \int_\Omega gH(-\varnothing)dx$. Where δ is the Dirac delta function and H represent the Heaviside function. g is edge indicator defined by $g(|\nabla f|) = \frac{1}{1+|\nabla G_\sigma * f|^2}$

3.3 Regularization term

In Eq. 4 $R_p(\varnothing)$ is the level set regularization term also called penalty term. By incorporating a regularization term, we ensure the maintenance of the signed distance property of our evolving surface wich uphold numerical stability:

$$R_p(\varnothing) \triangleq \int_\Omega p(|\nabla\varnothing|)dx \tag{6}$$

The potential function p:[0,∞)→R is required to have minimum points at s = 0 and s = 1, making it a double-well potential. The specific form is given by:

$$p_2(\mathrm{s}) = \begin{cases} \frac{1}{(2\pi)^2}(1-\cos(2\pi s)) & if\ s \le 1 \\ \frac{1}{2}(\mathrm{s}-1)^2, & if\ s \ge 1. \end{cases} \tag{7}$$

where $d_p(s) = p_2'(s)/s$ satisfies $\left|d_p(s)\right| < 1$ and $\lim_{s\to 0} d_p(s) = \lim_{s\to\infty} d_p(s) = 1$. Here $p_2{'}(s)$ is the derivative of $p_2(s)$. Consequently $\left|\mu d_p(|\nabla\varnothing|\right| \le \mu$, ensuring boundedness of the diffusion rate.

With both regularization and external energy terms included, the energy functional in Eq. 4 can be rewritten as follows:

$$\varepsilon(\varnothing) = \mu\int_\Omega p(|\nabla\varnothing|)dx + \lambda\int_\Omega g\delta(\varnothing)|\nabla\varnothing|dx + \alpha\int_\Omega gH(-\varnothing)dx$$

The constants μ, λ and α act as weights for each of the terms in our energy functional. For the potential p_2. We can write (4) as:

$$\frac{\partial\varepsilon}{\partial\varnothing} = \mu\frac{\partial R_p}{\partial\varnothing} + \frac{\partial\varepsilon_{ext}}{\partial\varnothing} \tag{8}$$

Based on Eq. 3 we can write:

$$\frac{\partial\varnothing}{\partial t} = -\mu\frac{\partial R_p}{\partial\varnothing} - \frac{\partial\varepsilon_{ext}}{\partial\varnothing} \tag{9}$$

The resulting distance regularized level set evolution is expressed as:

$$\frac{\partial\varnothing}{\partial \mathrm{t}} = \mu div\left(d_p(|\nabla\varnothing|)\nabla\varnothing\right) - \frac{\partial\varepsilon_{ext}}{\partial\varnothing} \tag{10}$$

This formulation (10) serves as a basis for image segmentation applications, incorporating edge-based information g.

The functional energy $\varepsilon(\varnothing)$ can be minimized by solving the following gradient flow:

$$\frac{\partial\varnothing}{\partial t} = \mu div\left(d_p(|\nabla\varnothing|)\nabla\varnothing\right) + \lambda\delta(\varnothing)div\left(g\frac{\nabla\varnothing}{|\nabla\varnothing|}\right) + \alpha g\delta(\varnothing) \tag{11}$$

This model (11) represents an edge-based geometric active contour, specifically tailored for image segmentation, with the advantage of distance regularization eliminating the need for re-initialization.

3.4 Proposed method

In level set models, an edge detector is employed to halt curve evolution at object boundaries, typically using a positive and regular edge function:

$$g(|\nabla f|)$$

Where $\lim_{t\to\infty} g(t) = 0$ and $g(|\nabla f|) = \frac{1}{1+|\nabla G_\sigma * f|^2}$ with $G_\sigma(x,y) = \sqrt{\sigma}\exp\left(-\frac{|x^2+y^2|}{4\sigma}\right)$. Where $G_\sigma * f$ is the convolution of the image f with the Gaussian kernel (G, σ), which give a smoother version of the image.

The edge function $g(|\nabla f|)$ is strictly positive in homogeneous regions and approaches zero near edges. Traditional active contour models rely on this edge function, which depends on the image gradient to halt curve evolution [34]. However, discrete gradients during implementation may be limited, resulting in the stopping function $g(|\nabla f|)$ never reaching zero at edges, potentially causing the curve to exceed boundaries, especially in heavily noisy images [36].

To address these limitations, a novel approach is proposed to integrate image restoration and segmentation simultaneously. The challenge of selecting an appropriate variance σ for the Gaussian kernel is acknowledged, where excessive smoothing can lead to loss of image edges, while insufficient smoothing is influenced by noise, impacting segmentation quality.

The proposed method aims to estimate the image f, reduce noise, and preserve edge details for accurate segmentation [48]. An anisotropic smoothing based on Euler's equation is introduced, alongside a regularization method with contour preservation [49]. The image estimation equation is expressed as:

$$H^*(y - Hf) + \beta div(K\nabla f) = 0 \tag{12}$$

where f and y represent vectors containing the true and observed images, respectively, H is the observation matrix, β is a regularization parameter, and K enables the preservation of discontinuities. Euler's equation is associated with the minimization criterion:

$$J(f) = \int |y - Hf|^2 + \beta^2 \int \varphi(|\nabla f|)| \tag{13}$$

φ is a regularizing function, and $K = \frac{\varphi\prime(|\nabla f|)}{2|\nabla f|}$

Equation (10) is analogous to anisotropic diffusion [50, 51], with $K = c(|\nabla f|)$ is the coefficient of heat transmission. depending on contours calculated by (1). Consider the function, $K = k(\varnothing)$ where the function $k(\varnothing)$ satisfies the following conditions: $k(\varnothing)$ is close to 0 near C (where C is represented as a level set of a function $\varnothing$), and it is near 1 elsewhere. The function k evolves simultaneously as the algorithm converges.

Initially, the contour determined by C is not well-localized, causing k to be a blurred version of $\varnothing$, so $k(\varnothing)$ away from C and slowly decreases to 0 near C. As the convergence of the algorithm progresses, C tends toward the contours of objects, and k tend to a Boolean function where $k(\varnothing)$ =0 on C (the contours) and $k(\varnothing)$ =1 in homogeneous areas of the image. To achieve this, a continuous function is employed that checks for the localization of contours and the homogeneity of regions in the image.

$$\begin{cases} k(\varnothing) = 1\, if\ \varnothing \geq e \\ k(\varnothing) lineare\ 0 < \varnothing < e \\ k(0) = 1 - \frac{1}{e} \end{cases} \tag{14}$$

The Boolean function approaches completion as the algorithm evolves, with the value of "e" gradually decreasing toward 1. The ultimate outcome is a Boolean function when "e" equals 1.

By coupling (11) with (12), the new system of two PDE is:

$$\frac{\partial \varnothing}{\partial t} = \mu div\left(d_p(|\nabla\varnothing|)\nabla\varnothing\right) + \lambda\delta(\varnothing) div\left(g\frac{\nabla\varnothing}{|\nabla\varnothing|}\right) + \alpha g\delta(\varnothing) \tag{15a}$$

$$\frac{\partial f}{\partial t} = H^*(y - Hf) + \beta div(k(\varnothing)\nabla f) \tag{15b}$$

With predefined boundary conditions, the edge stop function is expressed as $g(|\nabla f|) = \frac{1}{1+|\nabla f/\gamma|^2}$, where γ sets the gradient threshold for object detection.

Proposed method: Algorithm processes

$\frac{\partial f}{\partial t} = H^*(y - Hf) + \beta div(k(\emptyset)\nabla f)$ ⟶ processes the image f according to $\emptyset$

$\frac{\partial \emptyset}{\partial t} = \mu div\left(d_p(|\nabla\emptyset|)\nabla\emptyset\right) + \lambda\delta(\emptyset) div\left(g\frac{\nabla\emptyset}{|\nabla\emptyset|}\right) + \alpha g\delta(\emptyset)$ ⟶ processes the image distances $\emptyset$ of c according to

➛ Repeat until convergence on f and $\emptyset$

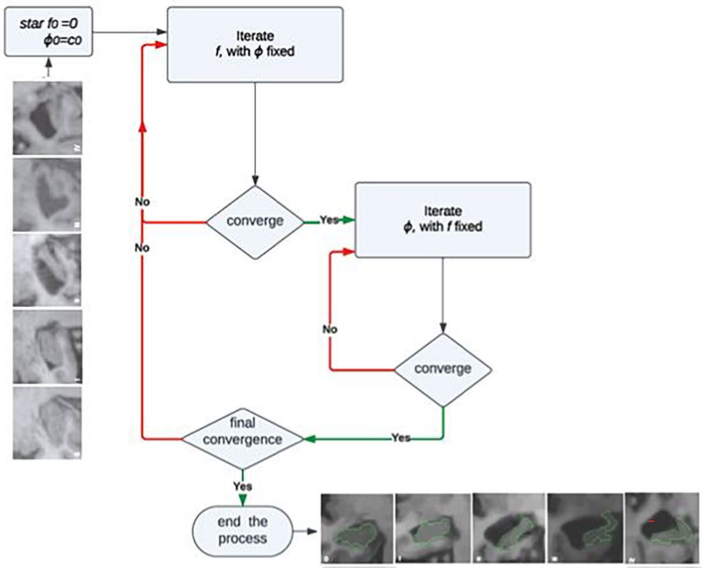

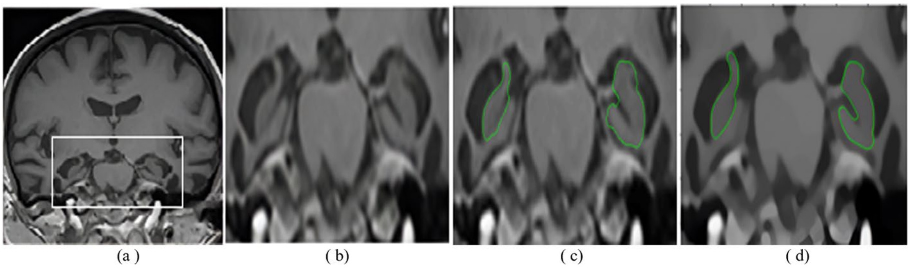

Fig. 1 The results of the segmentation of the hippocampus correspond to a subject with Alzheimer's(advanced stage). (**a**) The irm image in **Coronal view**, (**b**) Zoom on the segmented region (**c**) Image segmented with drlse model (**d**) Image segmented with our proposed approach

4 Results and discussion

The experimental environment is Matlab R2014b installed onto a PC Intel (R) Core i3 CPU, 2.40 GHz, 4 GB RAM. To prove the positive effect of proposed method, we randomly choose samples from EADC-ADNI dataset Harmonized Protocol for Hippocampal Segmentation (www.hippocampal-protocol.net) [52] and subjectively compare the segmentation results of the proposed method with the previous level set method and the drsle method.

In this section, several brain MRI images are used. To assess the robustness of the proposed approach, visual and quantitative experiments were performed on these images. There are parameters μ, λ and α in this model, and the time step Δt for the implementation, where:

μ is coefficient of the level set regularization term, λ is coefficient of the weighted length term $\mathcal{L}_g(\varnothing)$ that contains Dirac delta function, α represent coefficient of the weighted area term $\mathcal{A}_g(\varnothing)$ that contains Heaviside function, ε is parameter that specifies the width of the Dirac Delta function, and σis scale parameter in Gaussian kernel.

The choice of λ and μ can be fixed for the majority of applications, as the model demonstrates insensitivity to their variation. We set $\lambda=5$, $\mu=0.04$, $\Delta t=5$ and α is variable depends on the image used. and needs to be tuned for different images. The parameter β is manually tuned.

In the first experimental, segmentation is applied to MRI images in coronal, sagittal and Axial view. Figure 1 presents results of the segmentation of the hippocampus in coronal view correspond to a subject with Alzheimer's disease in advanced stage. In this experiment our approach is compared with distance regularized level set evolution model (drlse) [40]. It is clearly seen that drlse model fails to settle on the correct boundary, see Fig. 1(b). it is outstanding an overshoot of the contours on the two left and right globes of the hippocampus.

Figure 2 shows the segmentation results of the above two methods and our methods: (a) The segmentation result of level set method; (b) the segmentation result of [40], (c) the segmentation of the proposed method. The segmentation have serious boundary leakage in (a) and (b), while the results of our method are close to the ground truth.

Figure 3 presents results of the segmentation of the hippocampus in transverse vieuw. Figure 3 shows the segmentation results of the drsle method in [40] and in [53] and the proposed method: (a) The segmentation result of the contour draw by expert; (b) the drlse

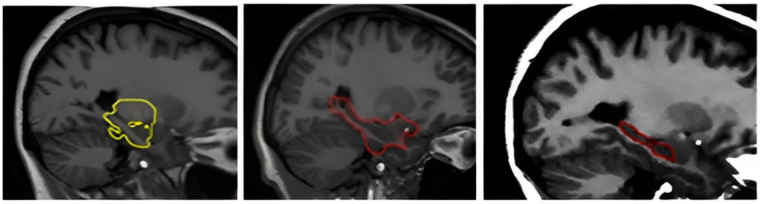

Fig. 2 The positive effect of shape prior. (**a**) Results of the level set method; (**b**) results of the method in [40]; (**c**) results of our method. **Sagittal vieuw**

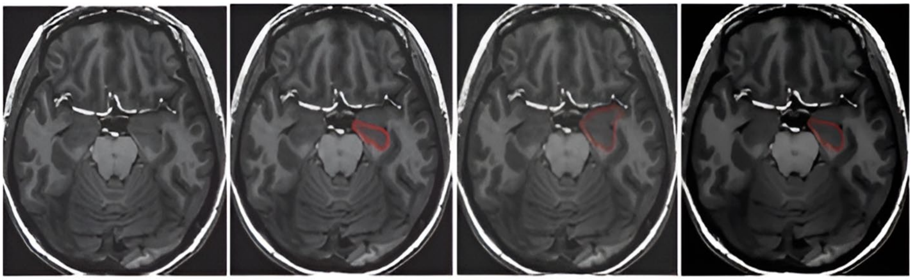

Fig. 3 (**a**) Input image (**b**) The segmentation result of the contour draw by expert; (**c**) the drlse method; (**d**) the result of the segmentation of the proposed method. **Axial vieuw**

method; (c) the segmentation result of [53] — in the drlse method the segmentation result has serious boundary leaks; we used the result in [53] to compare the accuracy of this segmentation with the proposed method. and (d) the result of the segmentation of the proposed method. we can see that DRLSE methods cannot segment HC correctly, while the results of our method compared with results in [53] are close to the ground truth.

In Fig. 4 Subject1, Subject2, and Subjet3 are three example subjects randomly selected from the baseline T1-weighted structural MRI data collected from 80 Alzheimer's Disease (AD), 135 MCI(Mild cognitive impairment), 121 Normal Control (NC) subjects in the Alzheimer's Disease Neuroimaging Initiative (ADNI) database.

4.1 Evaluation metrics for segmentation results

In order to quantitatively compare the effectiveness of segmentation, several techniques are used based on coefficients and indices. in this paper we used the Dice similarity coefficient, the Jaccard index (JI), sensitivity, FPR and FNR.

$$DSC = \frac{2TP}{2TP+FP+FN},\ Jaccard = \frac{TP}{TP+FP+FN},\ \text{Sensitivity} = \frac{TP}{TP+FN}$$

$$FPR = \frac{FP}{FP+TN}.$$

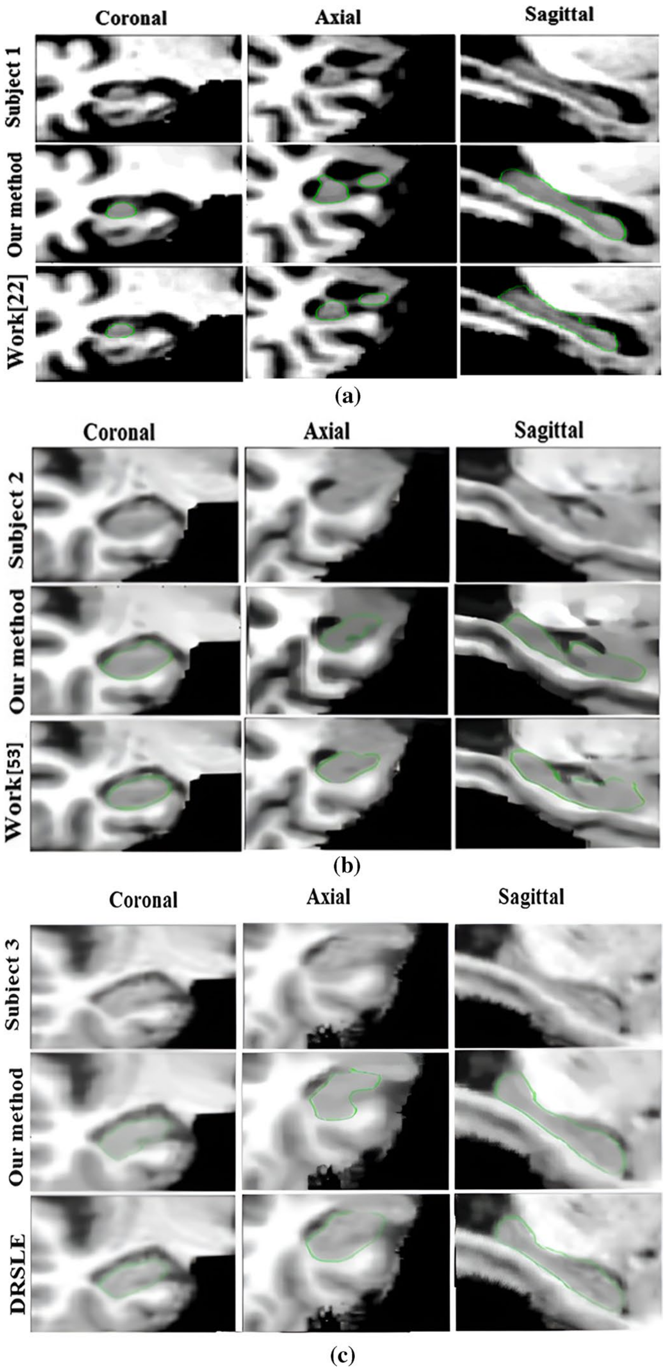

Fig. 4 **a** Comparison of segmented hippocampal regions by different methods for three example subjects from the test data. Shown coronal view, sagittal view, axial view. **b** Comparison of segmented hippocampal regions by different methods for three example subjects from the test data. Shown coronal view, sagittal view, axial view. **c** Comparison of segmented hippocampal regions by different methods for three example subjects from the test data. Shown coronal view, sagittal view, axial view

Table 1 Computed average Values of Jaccard, Dice, Sensitivity, FPR

Average	**Jacard**	**Dice**	**sensitivity**	**FPR**
Subj1				
Our method	0.9996	0.9112	0.9998	0.0002
Work [21]	0.7234	0.8392	0.7537	0.0303
Average	**Jacard**	**Dice**	**Sensitivity**	**FPR**
Subj2				
Our method	0.9815	0.8913	0.9827	0.0012
Work[53]	0.8794	0.8315	0.8798	0.0004
Average	**Jacard**	**Dice**	**Sensitivity**	**FPR**
Subj3				
Our method	0.9983	0.9215	0.9992	0.0009
Drsle	0.6538	0.7809	0.8831	0.2293

where TP denotes the true positives, FP denotes the false positives,; FN denotes the false negatives and TN true negatives.

The experimental results obtained in this section are represented in Table 1.

From Figs. 1, 2, 3 and 4, and Table 1 it can be concluded that the proposed algorithm has the ability to provide good image segmentation. which makes it possible to achieve high contour precision for noisy medical images.

4.2 Second experimental

To show the effectiveness of the proposed method, we will proceed to calculate the volume of the hippocampus using the LSF function and the result obtained will be compared with real results.

For this, we apply the proposed method with the Scheltens scale for the calculation of the hippocampus volume.

The Scheltens scale or medial temporal lobe atrophy (MTA) score is useful in distinguishing patients with Alzheimer's disease from those without disorders. The MTA score should be assessed on a slice through the hippocampal corpus on coronal T1-weighted images. This scale is based on a visual score of the width of the choroid fissure, the width of the temporal horn and the height of the hippocampal formation. The Scheltens Scale is widely used in clinical settings as well as in research studies to provide an objective measure of brain atrophy in patients with dementia. It can help in the diagnosis and monitoring of the progression of Alzheimer's disease. The scale ranges from 0 to 4, scale 0 indicates no atrophy and scale 4 indicates severe atrophy. Assessments are based on visual comparisons with reference images, taking into account the size and shape of specific brain regions. Figure 5 shows an example of the Scheltens scale [54].

While the Scheltens scale relies on visual inspection and subjective rating, segmentation provides a more quantitative and objective assessment by measuring the volumes or sizes of specific brain structures. Segmentation can be used alongside the Scheltens scale to complement the visual assessment with precise measurements. It's important to note that both the Scheltens scale and segmentation play important roles in neuroimaging research and clinical practice, providing valuable information about the severity of atrophy and enabling the study of disease progression and treatment effects. In the following experiment, the images in Fig. 6 are segmented using the proposed method to associate qualitative

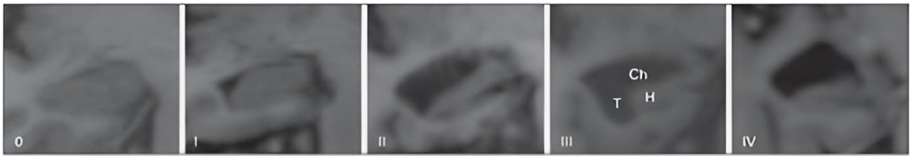

Fig. 5 Scheltens visual scale. Coronal T1-weighted MRI centered on the right hippocampus. Hippocampal atrophy graded by severity between 0 and IV from left to right. H hippocampus, T: temporal horn of the lateral ventricle, Ch: Choroid fissure

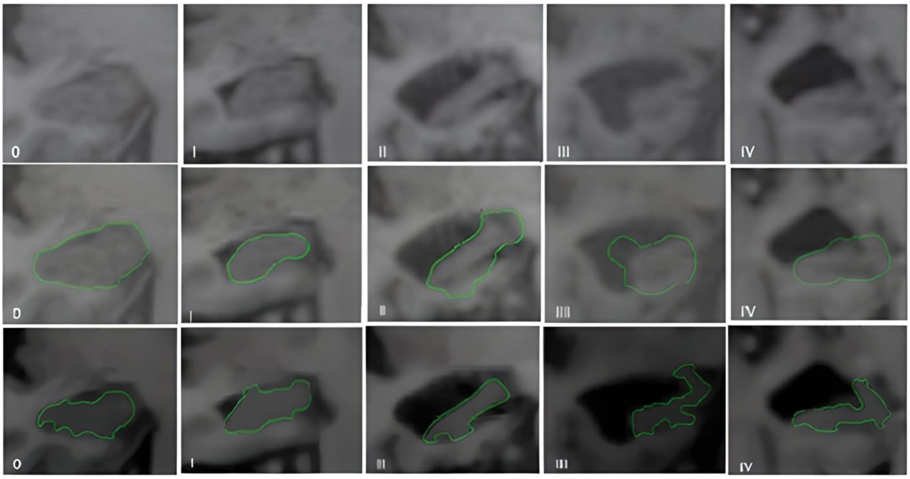

Fig. 6 First row: Scheltens visual scale. Coronal T1-weighted MRI centered on the right hippocampus. second row: result of the drlse method; third row:: proposed method segmentation

visual assessment with quantitative measurements. This allows for the comparison of subjective visual evaluations with objective volume measurements. By combining these two approaches, a better understanding can be obtained. Figure 6 shows the segmentation of images in the five situations on the Scheltens scale. The second row displays the segmentation result using DRLSE, which fails to segment accurately. The third row represents the result of the proposed method, which achieves the objective of the experiment. Figure 8 illustrates the segmentation by the proposed method for each image in Fig. 6, associated with the final level set function (LSF).

The experimental results obtained in this section are represented in Table 2. Table 3 addresses a quantitative comparison of the main methods for hippocampal segmentation in MRI using the Dice Similarity Coefficient (DSC).

Figure 7 displays the results outlined in Table 3.

5 Discussion

Table 3 addresses a quantitative comparison of the main methods for hippocampal segmentation in MRI using the Dice Similarity Coefficient (DSC). While it is possible to make this comparison, it is not feasible to assert that one method is the best for all types

Table 2 Scheltens visual scale. centered on the right hippocampus, Comparison between Dice index values

Dice	Dice1	Dice 1	Dice 3	Dice4	Dice 5	Average
Our method	0.908	0.912	0.925	0.921	0.923	0.918
Work [41]	0.881	0.870	0.887	0.791	0.799	0.845
R-Drsle [42]	0.865	0.878	0.889	0.841	0.815	0.857
O-Drsle [44]	0.887	0.897	0.905	0.881	0.850	0.884

of individuals because the rates presented in these publications are calculated on different quantities of images and on different types of individuals. In terms of accuracy, a DSC index of 0.80 can be considered a good value and has been used as a reference for the evaluation of automated methods, according to Fischl et al. 2002. This indicates that 80% of the segmented hippocampal region by the technique is accurate. Most of the methods presented have achieved or exceeded this rate, and some have shown significantly better rates. Among fully automated methods, the most accurate is presented by Wang et al. 2011, with a DSC index of 0.90. Among these methods, it is noteworthy to highlight the high similarity rate achieved by our method (dice = 91.8%).

To ensure the comprehensiveness of a research, it's recommended to conduct a thorough literature review to identify the most recent and relevant studies in the field of hippocampus segmentation. By combining insights from both older and more recent literature, researchers can gain a comprehensive understanding of the state-of-the-art methodologies and identify potential areas for further research and improvement. Figure 8 show segmentation results by proposed method for each image in Fig. 5 with final level set function (LSF).

While older references provide valuable insights, it's essential to acknowledge the currency of the literature and consider more recent studies or methodologies that might offer further advancements. In the context of research, exploring more recent studies could provide additional insights or improvements in hippocampus segmentation. These studies might leverage advancements in machine learning techniques, such as deep learning architectures, or incorporate novel imaging modalities and preprocessing techniques.

The inclusion of older references in Table 3, which provides a quantitative comparison of methods for hippocampus segmentation, serves multiple purposes despite the advancements in the field. Here's how older references contribute to the understanding of hippocampus segmentation:

1. Historical Context: Older references offer historical context, showcasing the evolution of methodologies and techniques in hippocampus segmentation. Understanding the progression of research allows for a deeper appreciation of current methodologies and their improvements over time.

Table 3 Quantitative comparison of methods for hippocampus segmentation

Author	Method(s)	DSC (average ± standard deviation)
Fischl et al. 2002	Probabilistic-Atlas	0.80
de Alejo et al. 2003	Neural Network	0.80 ± 0.70
Klemencic et al. 2004	AAM	0.80 ± 0.05
Carmichael et al. 2005	Single-Atlas	0.71
Heckemann et al. 2006	Multi-Atlas	0.84 ± 0.01
Chupin et al. 2007	Region Growing	0.84 ± 0.03
Han and Fischl 2007	Probabilistic-Atlas	0.83
Barnes et al. 2008	Multi-Atlas	0.86 ± 0.05
Van der Lijn et al. 2008	Probabilistic-Atlas	0.86 ± 0.03
Chupin et al. 2008	AAM	0.86 ± 0.03
Artaechevarria et al. 2009	Automatic Multi-Atlas	0.75
Collins and Pruessner 2010	Multi-Atlas	0.88
Wang et al. 2011	Multi-Atlas, Classifier	0.90
Atho et al. 2011	Cloud Model	0.86 ± 0.05
Bishop et al. 2011	ASM	0.81 ± 0.01
Kim et al. 2013	Probabilistic-Atlas	0.89 ± 0.02
Cardoso et al. 2013	Multi-Atlas	0.90
Hao et al. 2014	Multi-Atlas	0.89
Inglese P et al.2015	RFmulti classifier	0.87 ± 0.03
Qiang Zheng et al.2018	MULTI-ATLAS RF-SSLP	0.891 ± 0.01
Manhua Liu et al. 2020	automatic segmentation	0. 87
C. Ren et al. 2022	automatic segmentation	0. 901
Yang Lei Yifu.Ding et al. 2023	Deep learning segmentation	0.900 ± 0.029
Juan Jiang, Hong Liu et al. 2023	3D U-Net	0.878
Proposed method	A. level set method	0.918

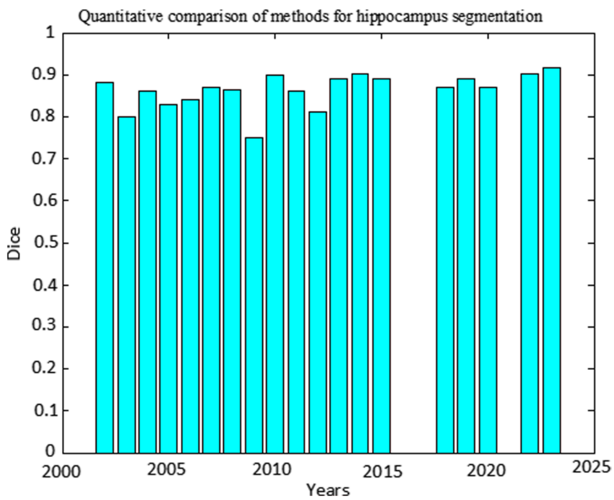

Fig. 7 Quantitative comparison of methods for hippocampus segmentation

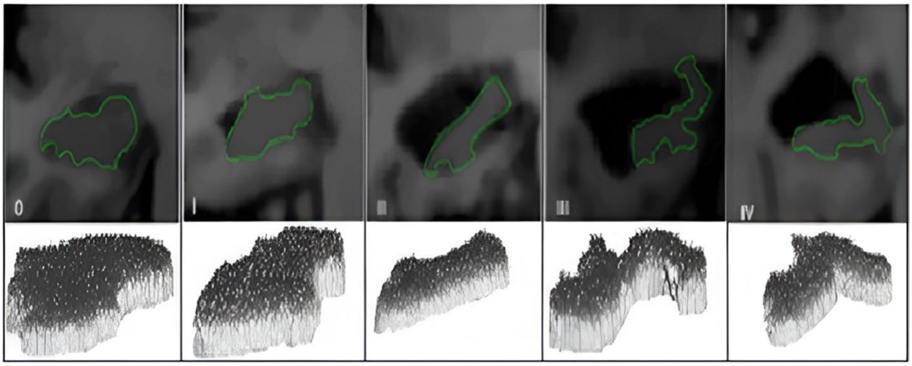

Fig. 8 the segmentation by the proposed method for each image in Fig. 5 associated with its forms represented by the final level set function (LSF)

2. Baseline Comparisons: Older studies often establish baseline methodologies or benchmarks against which newer methods can be compared. By including these references, researchers can assess how far the field has progressed and whether newer approaches offer significant improvements over established techniques.
3. Methodological Comparison: Although newer methods may offer superior performance, comparing them with older techniques can highlight the strengths and weaknesses of different approaches. This comparison aids in identifying the aspects that newer methodologies have improved upon and areas where further enhancements are needed.
4. Validation and Benchmarking: Many older references have been extensively validated and benchmarked using established datasets. Incorporating these studies into the comparison provides a basis for evaluating the performance of newer methods on standardized datasets, ensuring fair comparisons across different approaches.

5.1 Volume calcul

To calculate the volume using the LSF, one approach is to perform a numerical integration over the domain where the LSF is positive. The integral of the LSF over this domain represents the volume of the object. To demonstrate the link between the final level set function (LSF) and the volume of an object, we can use a mathematical approach based on integration. Let's assume we have an LSF $\varphi(x, y, z)$ that represents the boundary of an object in three-dimensional space.

To calculate the volume of the object from the LSF, we will numerically integrate the level set function over the region where it is positive (inside the object). The absolute value of the LSF is often used to obtain a positive representation of the function. Thus, we can define the positive function $g(x, y, z)$ as follows:

$$g(x, y, z) = |\varphi(x, y, z)|$$

Now, to calculate the volume of the object, we need to integrate the function $g(x, y, z)$ over the region inside the object. Let's assume that this region is bounded by a domain D in three-dimensional space.

Table 4 Scheltens visual scale. Coronal T1-weighted MRI centered on the right hippocampus,. volumes

Images	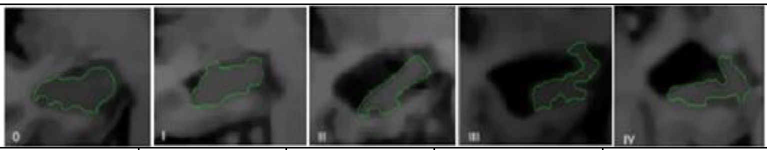				
Volume Cm^3	3.19	2.96	2.15	1.645	1.289

Table 5 Comparison between right hippocampal volumes in different methods

Method	Right hippocampus volume
In [55]	3.05 cm^3
In [56]	3.39 cm^3
Proposed method	3.19 cm^3

The volume V of the object can be calculated using the following triple integral:

$$V = \int\int\int \_Dg(x, y, z)dv$$

where dv represents the infinitesimal volume element in the coordinates (x, y, z).

The triple integration can be performed using appropriate numerical integration techniques. By performing this numerical integration, we obtain an estimation of the volume of the object from the LSF. The experimental results obtained in this section are represented in Table 4. Table 5 provides a comparison between the proposed method and other methods.

6 Conclusion

This study proposes an efficient and innovative approach for the segmentation of the hippocampus in MRI images, addressing the challenges posed by its small size, complex shape, and low contrast characteristics. The methodology involves modeling and solving a system of two-dimensional partial differential equations, incorporating anisotropic smoothing and adaptive level set methods. The iterative application of these equations results in a new algorithm that overcomes limitations observed in previous models. The proposed method is evaluated for hippocampus volume calculation using the Scheltens scale, and the results demonstrate its clinical utility. Comparative analyses with manual segmentations performed by expert radiologists reveal a Dice similarity rate averaging 91.8%. The volume values obtained align well with established standards, ranging between 3.19 cm3 and 1.3 cm3 for the right hippocampus. These outcomes signify a substantial improvement in both quantity and quality compared to existing models in the field, establishing the credibility and efficacy of the developed approach. In summary, the presented methodology proves to be a contribution to the field of hippocampus segmentation in neuroimaging, showcasing performance and potential clinical applicability. The accuracy and reliability demonstrated in this study position the proposed algorithm as a promising tool for early detection and monitoring of diseases such as Alzheimer's, where hippocampal changes serve as crucial indicators.

Acknowledgements We would like to thank Dr. Yasser .r. Haddadi.

Availability of data and materials Not applicable.

Declarations

Ethical approval and consent to participate Not applicable.

Human ethics Not applicable.

Conflict of interest The authors declare that they have no conflict of interest.

References

1. Yushkevich PA, Wang HZ, Pluta J, Das SR, Craige C, Avants BB, Weiner MW, Mueller S (2011) Nearly automatic segmentation of hippocampal subfields in in vivo focal T2-weighter MRI. Neuroimage 53(4):1208–1224. https://doi.org/10.1016/j.neuroimage.2010.06.040
2. Treves A, Rolls ET (1994) Computational analysis of the role of the hippocampus in memory. Hippocampus 4(3):374–391. https://doi.org/10.1002/hipo.450040319
3. Fortin NJ, Agster KL, Eichenbaum HB (2002) Critical role of the hippocampus in memory for sequences of events. Nat Neurosci 5(5):458–462. https://doi.org/10.1038/nn834
4. Rubin RD, Watson PD, Duff MC et al (2014) The role of the hippocampus in flexible cognition and social behavior. Front Human Neurosci 8:742. https://doi.org/10.3389/fnhum.2014.00742
5. Anand KS, Dhikav V (2012) Hippocampus in health and disease: an overview. Ann Indian Acad Neurol 15:239. https://doi.org/10.4103/0972-2327.104323
6. Geuze E, Vermetten E, Bremner J (2005) MR-based in vivo hippocampal volumetrics: 2 Findings in neuropsychiatric disorders. Mol Psychiatry 10:160. https://doi.org/10.1038/sj.mp.4001579
7. Guo J, Feng X, Zhou S, Yan W, Meng D (2016) Potential anti-Alzheimer's disease activities of the roots of Desmodium caudatum. Ind Crops Prod 90(15):94–99. https://doi.org/10.1016/j.indcrop.2016.06.018
8. Chaalal A, Poirier R, Blum D et al (2014) PTU-induced hypothyroidism in rats leads to several early neuropathological signs of Alzheimer's disease in the hippocampus and spatial memory impairments. Hippocampus 24(11):1381–1393. https://doi.org/10.1002/hipo.22319
9. Imparato F (2016) Celiac disease could have been the cause of Caesar's epilepsy. J Clin Gastroenterol 50(9):797. https://doi.org/10.1097/MCG.0000000000000558
10. Wang B, Meng L (2016) Functional brain network alterations in epilepsy: a magnetoencephalography study. Epilepsy Res 126:62–69. https://doi.org/10.1016/j.eplepsyres.2016.06.014
11 Troubé S (2016) Philosophy of psychiatry and phenomenology of everyday life: the disruptions of ordinary experience in schizophrenia. Revue de Synthese 137(1–2):61–86. https://doi.org/10.1007/s11873-016-0291-9
12. Pinacho R, Valdizán EM, Pilar-Cuellar F et al (2014) Increased SP4 and SP1 transcription factor expression in the postmortem hippocampus of chronic schizophrenia. J Psychiatric Res 58:189–196. https://doi.org/10.1016/j.jpsychires.2014.08.006
13. Jack CR Jr, Shiung MM, Gunter JL et al (2004) Comparison of different MRI brain athrophy Rate measures with clinical disease progression in AD. Neurology 62(4):591–600. https://doi.org/10.1212/01.wnl.0000110315.26026.ef
14. Bobinski M (1996) Neurofibrillary pathology—correlation with hippocampal formation atrophy in Alzheimer disease. Neurobiol Aging 17(6):909–919. https://doi.org/10.1016/s0197-4580(96)00160-1
15. Dill V, Franco AR, Pinho MS (2015) Automated Methods for Hippocampus Segmentation: the Evolution and a Review of the State of the Art. Neuroinform 13:133–150. https://doi.org/10.1007/s12021-014-9243-4
16. Csernansky JG, Joshi S, Wang L, Haller JW, Gado M, Miller JP, Miller MI (1998) Hippocampal morphometry in schizophrenia by high dimensional brain mapping. Proc Natl Acad Sci 95(19):11406–11411. https://doi.org/10.1073/pnas.95.19.11406
17. Li BN, Chui CK, Chang S, Ong SH (2011) Integrating spatial fuzzy clustering with level set methods for automated medical image segmentation. Comput Biol Med 41(1):1–10. https://doi.org/10.1016/j.compbiomed.2010.10.007

18 Maulik U, Bandyopadhyay S (2000) Genetic algorithm-based clustering technique. Pattern Recogn. 33:1455–1465. https://doi.org/10.1016/S0031-3203(99)00137-5
19. Chama Z, Mansouri B, Anani M, Mohammad-Djafari Ali (2012) Image recovery from fourier domain measurements via classification using bayesian approach and total variation regularization. Int J Electron Commun 66(3):897–902. https://doi.org/10.1016/J.Aeue.2012.03.008
20. Liu B, Cheng HD, Huang J, Tian J, Tang X, Liu J (2010) Probability density difference-based active contour for ultrasound image segmentation. Pattern Recognit 3(2):2028–2042. https://doi.org/10.1016/J.Patcog.2010.01.002
21. Mansouri B, Haddadi Y, Chama Z, Djafari AM (2019) Image reconstruction based on bayesian total variation and hidden markov model. In 2019 6th International Conference on Image and signal Processing and their Applications (ISPA) (pp 1–5). IEEE. https://doi.org/10.1109/ISPA48434.2019.8966879
22 Liu Y, Yan Z (2020) A combined deep-learning and lattice boltzmann model for segmentation of the hippocampus in MRI. Sensors 20(13):3628. https://doi.org/10.3390/s20133628
23. Bozkurt F, Köse C, Sarı A (2020) A texture-based 3D region growing approach for segmentation of ICA through the skull base in CTA. Multimedia Tools Appl 79:33253–33278. https://doi.org/10.1007/s11042-020-09690-z
24. Liu M, Li F, Yan H, Wang K, Ma Y, Shen L, …, Alzheimer's Disease Neuroimaging Initiative (2020) A multi-model deep convolutional neural network for automatic hippocampus segmentation and classification in Alzheimer's disease. Neuroimage 208:116459
25. Tao C, Gu D, Huang R, Zhou L, Hu Z, Chen Y, …, Li H (2023) Hippocampus segmentation after brain tumor resection via postoperative region synthesis. BMC Medical Imaging 23(1):142. https://doi.org/10.1186/s12880-023-01087-2
26. An FP, Je Liu (2021) Medical image segmentation algorithm based on multilayer boundary perception-self attention deep learning model. Multimed Tools Appl 80:15017–15039. https://doi.org/10.1007/s11042-021-10515-w
27. Li JN, Zhang SW, Qiang YR, Zhou QY (2023) A novel cross-layer dual encoding-shared decoding network framework with spatial self-attention mechanism for hippocampus segmentation. Comput Biol Med 167:107584. https://doi.org/10.1016/j.compbiomed.2023.107584
28. Inglese P, Amoroso N, Boccardi M, Bocchetta M, Bruno S, Chincarini A, Errico R, Frisoni GB, Maglietta R, Redolfi A et al (2015) Multiple RF classifier for the hippocampus segmentation: Method and validation on EADC-ADNI Harmonized Hippocampal Protocol. Phys Medica 31:1085–1091. https://doi.org/10.1016/j.ejmp.2015.08.003
29. He C, Li K, Zhang Y, Tang L, Zhang Y, Guo Z, Li X (2023) Camouflaged object detection with feature decomposition and edge reconstruction. IEEE Conference on Computer Vision and Pattern Recognition (CVPR). https://doi.org/10.48550/arXiv.2307.03943
30. He C, Li K, Zhang Y, Xu G, Tang L, Zhang Y, Guo Z, Li X (2023) Weakly-supervised concealed object segmentation with SAM-based pseudo labeling and multi-scale feature grouping. arXiv:2305.11003 [cs.CV]. https://doi.org/10.48550/arXiv.2305.11003
31. He C, Li K, Zhang Y, Zhang Y, Guo Z, Li X, Danelljan M, Yu F (2024) Strategic preys make acute predators: Enhancing camouflaged object detectors by generating camouflaged objects. arXiv:2308.03166 https://doi.org/10.48550/arXiv.2308.03166
32. Caselles V, Morel JM, Sapiro G (1997) Geodesic active contours. Int J Comput 22(1):61–79. https://doi.org/10.1006/Cviu.1997.0562
33. Kass M, Witkin A, Terzopoulos D (1988) Snakes: Active contour models. Int J Comput Vision 1(4):321–331. https://doi.org/10.4236/1987.3521
34 Malladi R, Sethian JA, Vermuri BC (1995) Shape modeling with front propagation: A level set approach. IEEE Trans Pattern Anal Mach Intell 17(2):158–175. https://doi.org/10.1109/34.368173
35. AruniNiroshika UA, Ravinda GN, Meegama S, Ravindra S, Lokupitiya R, Donna Kannangara KS (2015) Active contours with prior corner detection to extract discontinuous boundaries of anatomical structures in x-ray images. IET Image Process 9(3):202–210. https://doi.org/10.1049/Iet-Ipr.2014.0106
36. Chen H, Zhang H, Zhen X (2023) A hybrid active contour image segmentation model with robust to initial contour position. Multimed Tools Appl 82:10813–10832. https://doi.org/10.1007/s11042-022-13782-3
37. Goldenberg R, Kimmel R, Rivlin E, Rudzsky M (2001) Scale space theories in computer vision. IEEE Trans Image Process 10(10):34–45. https://doi.org/10.1007/3-540-48236-9_4
38 Sethian J (1999) Level set methods and fast marching methods. Cambridge Univ Press, UK. https://doi.org/10.1017/S0263574799212404 (**Opens in a new window**)
39 Osher S, Fedkiw R (2002) Level Set Methods And Dynamic Implicit Surfaces. Springer-Verlag, New York. https://doi.org/10.1007/b98879

40. Chunming L, Chenyang X, Changfeng G, Martin Fox D (2010) Distance regularized level set evolution and its application to image segmentation. IEEE Trans Image Process 19(12):32433254. https://doi.org/10.1109/TIP.2010.2069690
41. Wu Y, He C (2015) Indirectly regularized variational level set model for image segmentation. Neurocomputing 171(4):194–208. https://doi.org/10.1016/J.Neucom.2015.06.027i
42 Yu C (2013) A novel active contour model for image segmentation using distance regularization term. Comput Math Appl 65(3):1746–1759. https://doi.org/10.1016/j.camwa.2013.03.021
43. Young JC, Afriliana N, Natalia F, Meidia H, Sudirman S (2019) A study on the suitability of applying active contour evolution models in segmenting ad delineating boundaries in medical images. The 5th International Conference on New Media Studies (CONMEDIA), pp. 232–237. https://doi.org/10.1109/CONMEDIA46929.2019.8981855
44. Liu P, Xu X (2020) Oriented distance regularized level set evolution for image segmentation. Int J Imaging Syst Technol 30(4):1–15. https://doi.org/10.1002/Ima.22452
45. Cai X (2015) Variational image segmentation model coupled with image restoration achievements. Pattern Recogn 48(6):2029–2042. https://doi.org/10.1016/j.patcog.2015.01.008
46. Larbi M, Messali Z, Rouini A, Larbi S (2019) An image segmentation model using a level set method based on improved signed pressure force function SPF. The 4th International Conference On Electrical Engineering And Control Applications, ICEECA, pp 17–19. Constantine. https://doi.org/10.1007/978-981-15-6403-1_87
47. Malladi R, Sethian JA (1996) Unified approach to noise removal, image enhancement and shape recovery. IEEE Trans on Image Processing 5(11):1554–1568. https://doi.org/10.1145/3368756
48. Kornprobst P, Deriche R (1996) Image Restoration via PDE, The Conference Investigative Image Processing, Part Of SPIE's First Annual Symposium On Enabling Technologies For Law Enforcement And Security, SPIE, Boston, MA
49. Blanc LF, Teboul S, Aubert G, Barlaud M (1996) Nonlinear Regularization Using Constrained Edges In Image Construction. IEEE The 3rd International Conference Of Image Processing, Vol. 2, pp 449–452, Lausanne. https://doi.org/10.1109/ICIP.1996.560882
50. Perona P, Scale J (1992) Space and edge detection using anisotropic diffusion. IEEE PAMI 12(7):629–639. https://doi.org/10.1234/35142686
51. Shah J (1996) Common Framework for Curve Evolution, Segmentation and Anisotropic Diffusion. IEEE Conference On Computer Vision And Pattern Recognition, pp 136–142, San Francisco. https://doi.org/10.1028/471398957
52. Boccardi M, Bocchetta M, Apostolova LG, Barnes J, Bartzokis G, Corbetta G, DeCarli C, deToledo-Morrell L, Firbank M, Ganzola R, Gerritsen L, Henneman W, Killiany RJ, Malykhin N, Pasqualetti P, Pruessner JC, Redolfi A, Robitaille N, Soininen H, Tolomeo D, Wang L, Watson C, Wolf H, Duvernoy H, Duchesne S, Jack CR Jr, Frisoni GB, EADC-ADNI Working Group on the Harmonized Protocol for Manual Hippocampal Segmentation (2015) Delphi definition of the EADC-ADNI Harmonized Protocol for hippocampal segmentation on magnetic resonance. Alzheimers Dement. 11(2):126–38. https://doi.org/10.1016/j.jalz.2014.02.009
53. Hajiesmaeili M, Bagherinakhjavanlo B, Dehmeshki J, Ellis T (2012) Segmentation of the Hippocampus for Detection of Alzheimer's Disease. In: , et al. Advances in Visual Computing. ISVC 2012. Lecture Notes in Computer Science, vol 7431. Berlin: Springer. https://doi.org/10.1007/978-3-642-33179-4_5
54. Combes D, Tanguy JY, Annweiler C, Labriffe M (2020) Imagerie normale et pathologique de l'hippocampe en gériatrie [Normal and pathological hippocampal imaging in geriatric patients]. Geriatr Psychol Neuropsychiatr Vieil. 18(1):7–18. https://doi.org/10.1684/pnv.2019.0819
55. Salmah Jalaluddin MW, Jusoh NM, Basahai IAA, Abdullah MS, Karim AHA, Gazali AK (2013) Normalised MRI volumetry of the hippocampus among normal malay children and adolescents. Malays J Med Sci 20(1):31–38
56. Embong MF, Yaacob R, Abdullah M, Abdul Karim AH, Ghazali AK, Mar W, Jalaluddin S (2013) MR volumetry of hippocampus in normal adult malay of age 50 years old and above. Malays J Med Sci 20(4):25–31

Authors and Affiliations

Boualem Mansouri[1] · Mohammed Chetioui[1] · Catherine Choquet[2] · Lakhdar Boumia[3] · Chama Zouaoui[4]

✉ Boualem Mansouri
mansourieln@yahoo.fr

1 Laboratory of Electronics, Advanced Signal Processing and Microwaves (LESM), Faculty of Technology, TM University TM of Saida, Saida, Algeria

2 MIA Laboratory, La Rochelle University, La Rochelle, France

3 LEIMA Laboratory, Faculty of Sciences, University of Tissemsilst, Tissemsilst, Algeria

4 Department of Electronics, University UDL of Sidi Bel Abbes, Sidi Bel Abbes, Algerie